Identical particles

Non-interacting particles (classical or distinguishable)

$$\hat{H}(\vec{r}_1, \vec{r}_2) = -\frac{\hbar^2}{2m_1}\nabla_1^2 - \frac{\hbar^2}{2m_2}\nabla_2^2 + V_1(\vec{r}_1) + V_2(\vec{r}_2)$$

$\psi(\vec{r}_1, \vec{r}_2)$ $\quad \hat{H}\psi(\vec{r}_1, \vec{r}_2) = E\psi(\vec{r}_1, \vec{r}_2)$

Separation of variables: $\psi(\vec{r}_1, \vec{r}_2) = \psi_1(\vec{r}_1)\psi_2(\vec{r}_2)$

$$\hat{H}\psi(\vec{r}_1, \vec{r}_2) = \left[-\frac{\hbar^2}{2m_1}\nabla_1^2\psi_1(r_1) + V_1(\vec{r}_1)\psi_1(\vec{r}_1)\right]\psi_2(r_2) + \left[-\frac{\hbar^2}{2m_2}\nabla_2^2\psi_2(\vec{r}_2) + V_2\psi_2(\vec{r}_2)\right]\psi_1$$

$$= E\psi_1\psi_2$$

$$-\frac{\hbar^2}{2m_1}\nabla^2\psi_1(\vec{r}_1) + V_1(\vec{r}_1)\psi_1(\vec{r}_1) = E_1\psi_1(\vec{r}_1)$$

$$-\frac{\hbar^2}{2m_2}\nabla^2\psi_2(\vec{r}_2) + V_2(\vec{r}_2)\psi_2(\vec{r}_2) = E_2\psi_2(\vec{r}_2)$$

} Single-particle Shrodinger eqns

$$E = E_a + E_b$$

Time-dependent wave function: $\psi(\vec{r}_1, \vec{r}_2) = \psi_a(\vec{r}_1)\,\psi_b(\vec{r}_2)\,e^{-i(E_a+E_b)t/\hbar}$

Probability density $P(r_1, r_2) = |\psi(\vec{r}_1, \vec{r}_2)|^2 = |\psi_1(r_1)|^2|\psi_2(\vec{r}_2)|^2 = P_1(\vec{r}_1)\cdot P_2(\vec{r}_2)$

Indistinguishable particle: $\hat{H}(1,2) = \hat{H}(2,1)$

here "1" or "2" describes each particle

Since particles are indistinguishable, nothing in the physical world should change when you switch them around:

must be: $P(\vec{r}_1, \vec{r}_2) = P(\vec{r}_2, \vec{r}_1) \Rightarrow |\psi(\vec{r}_1, \vec{r}_2)|^2 = |\psi(\vec{r}_2, \vec{r}_1)|^2 \Rightarrow$

$$\psi(\vec{r}_1, \vec{r}_2) = \pm\psi(\vec{r}_2, \vec{r}_1)$$

Thus, the wave function of two distinguishable particles must be either symmetric or anti-symmetric.

$$\psi_\pm(\vec{r}_1, \vec{r}_2) = \frac{1}{\sqrt{2}}\left(\psi_a(\vec{r}_1)\psi_b(\vec{r}_2) \pm \psi_a(\vec{r}_2)\psi_a(\vec{r}_1)\right)$$

More rigorous derivation

Let is introduce a particle interchange operator $\hat{P}_{1,2}$

$$\hat{P}_{1,2}\,\hat{H}(1,2) = \hat{H}(2,1) \qquad \hat{P}_{1,2}\,\psi(\vec{r}_1,\vec{r}_2) = \psi(\vec{r}_2,\vec{r}_1)$$

Now, $\hat{P}_{1,2}\left[\hat{H}(1,2)\,\psi(\vec{r}_1,\vec{r}_2)\right] = \hat{H}(2,1)\,\psi(\vec{r}_2,\vec{r}_1) =$

$= \hat{H}(2,1)\,\hat{P}_{1,2}\,\psi(\vec{r}_1,\vec{r}_2) = \hat{H}(1,2)\,\hat{P}_{1,2}\,\psi(\vec{r}_1,\vec{r}_2)$

non-distinguishable

$$\left(\hat{P}_{1,2}\hat{H}(1,2) - \hat{H}(1,2)\hat{P}_{1,2}\right)\psi(\vec{r}_1,\vec{r}_2) = 0$$

$$\left[\hat{P}_{1,2},\hat{H}(1,2)\right] = 0 \qquad \hat{P}_{1,2} \text{ and } \hat{H}(1,2) \text{ commute}$$

Thus $\psi(\vec{r}_1,\vec{r}_2)$ must be the eigenfunction of $\hat{P}_{1,2}$

$$\hat{P}_{1,2}\,\psi(\vec{r}_1,\vec{r}_2) = p\cdot\psi(\vec{r}_1,\vec{r}_2)$$

$$\psi(\vec{r}_1,\vec{r}_2) = \hat{P}_{1,2}\,\psi(\vec{r}_2,\vec{r}_1) = p\,\psi(\vec{r}_2,\vec{r}_1) = p^2\psi(\vec{r}_1,\vec{r}_2)$$

$$p^2 = \pm 1 \quad \Rightarrow \quad \psi_{\pm}(\vec{r}_1,\vec{r}_2) = \pm\,\psi(\vec{r}_2,\vec{r}_1)$$

With the operator approach, it is easier to generalize to multi-particle systems, for which the wave function will be symmetric or anti-symmetric under a ~~per~~ interchange of any two particles.

3 particles: $\psi(1,2,3) = \psi(2,1,3) = \psi(3,2,1) = \psi(1,3,2) = \psi(2,3,1) = \psi(3,1,2)$

↳ symmetric case

$$\psi(1,2,3) = -\psi(2,1,3) = -\psi(3,2,1) = -\psi(1,3,2) = \psi(2,3,1) = \psi(3,1,2)$$

Bosons: particles with symmetric wave function

$$\psi_+ = \frac{1}{\sqrt{2}}\left(\psi_a(\vec{r}_1)\psi_b(\vec{r}_2) + \psi_a(\vec{r}_2)\psi_b(\vec{r}_1)\right)$$

can be at the same single-particle quantum state

$\psi_+ = \psi_a(\vec{r}_1)\psi_a(\vec{r}_2)$ → obviously symmetric!

Fermions: particles with anti-symmetric wave function

$$\psi_- = \frac{1}{\sqrt{2}}\left(\psi_a(\vec{r}_1)\psi_b(\vec{r}_2) - \psi_a(\vec{r}_2)\psi_b(\vec{r}_1)\right)$$

if $a = b$ $\psi_- \equiv 0$ (i.e. such situation is impossible)

(Pauli exclusion principle)

Example: two non-interacting particles in an infinite square well
(as two neutral atoms in an optical trap)

Distinguishable particles:

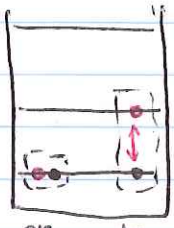

Ground state: $\psi_{gr}(x_1,x_2) = \frac{2}{L}\sin\frac{\pi x_1}{L}\sin\frac{\pi x_2}{L}$

$E_{gr} = 2\cdot\frac{\pi^2\hbar^2}{2mL^2} = 2E_0$

First excited state

$\psi_{1e}(x_1,x_2) = \frac{2}{L}\sin\frac{\pi x_1}{L}\sin\frac{\pi x_2}{2L}$

or

$\frac{2}{L}\sin\frac{\pi x_2}{L}\sin\frac{\pi x_1}{2L}$

$E_{1e} = E_0 + 4E_0 = 5E_0$

Bosons: $\psi_{gr}^{(bosons)} = \psi_{gr} = \frac{2}{L}\sin\frac{\pi x_1}{L}\sin\frac{\pi x_2}{L}$ $\quad E_{gr}^{(boson)} = 2E_0$

$$\psi_{1e}^{(boson)} = \frac{2}{L}\left(\sin\frac{\pi x_1}{L}\sin\frac{\pi x_2}{2L} + \sin\frac{\pi x_2}{L}\sin\frac{\pi x_1}{2L}\right) \quad E_{1e}^{(boson)} = 5E_0$$

Fermions: $\psi_{gr}^{(ferm)} = \frac{2}{L}\left(\sin\frac{\pi x_1}{L}\sin\frac{\pi x_2}{2L} - \sin\frac{\pi x_2}{L}\sin\frac{\pi x_1}{2L}\right)$ $\quad E_{gr}^{(ferm} = 5E_0$

How do we know if a particle is a fermion or a boson?
It's statistics is determined by its spin

Integer spin particles → bosons
photons, ~~gravitons~~ gluons, Z and W-bosons, Higgs

Half-integer spin particles → fermions
electrons, protons, neutrons, ..
on a more fundamental level: leptons (e, μ, τ + ν_e, ν_μ, ν_τ + their anti-particles)
quarks plus anti-quarks.

Hadrons:
Composite particles
Mesons: elementary particles containing a quark and an anti-quark → integer spin → boson
Baryons: elementary particles containing 3 valence quarks (and anti-quarks) → half-integer spin → fermions

Even more complex composite particles
$^3He^{2+}$ = p+p+n → 3 fermions spin 1/2 → fermions
$^4He^{2+}$ = p+p+n+n → 4 fermions spin 1/2 → boson

Still, the statistics depends on total spin
Fermion atom – sum of all neutrons, protons and electrons is an odd number
Boson atom – sum of all neutrons, protons and electrons is an even number

^{87}Rb	($Z = 37$, $N = 40$)	boson
^{40}K	($Z = 19$, $N = 21$)	fermion

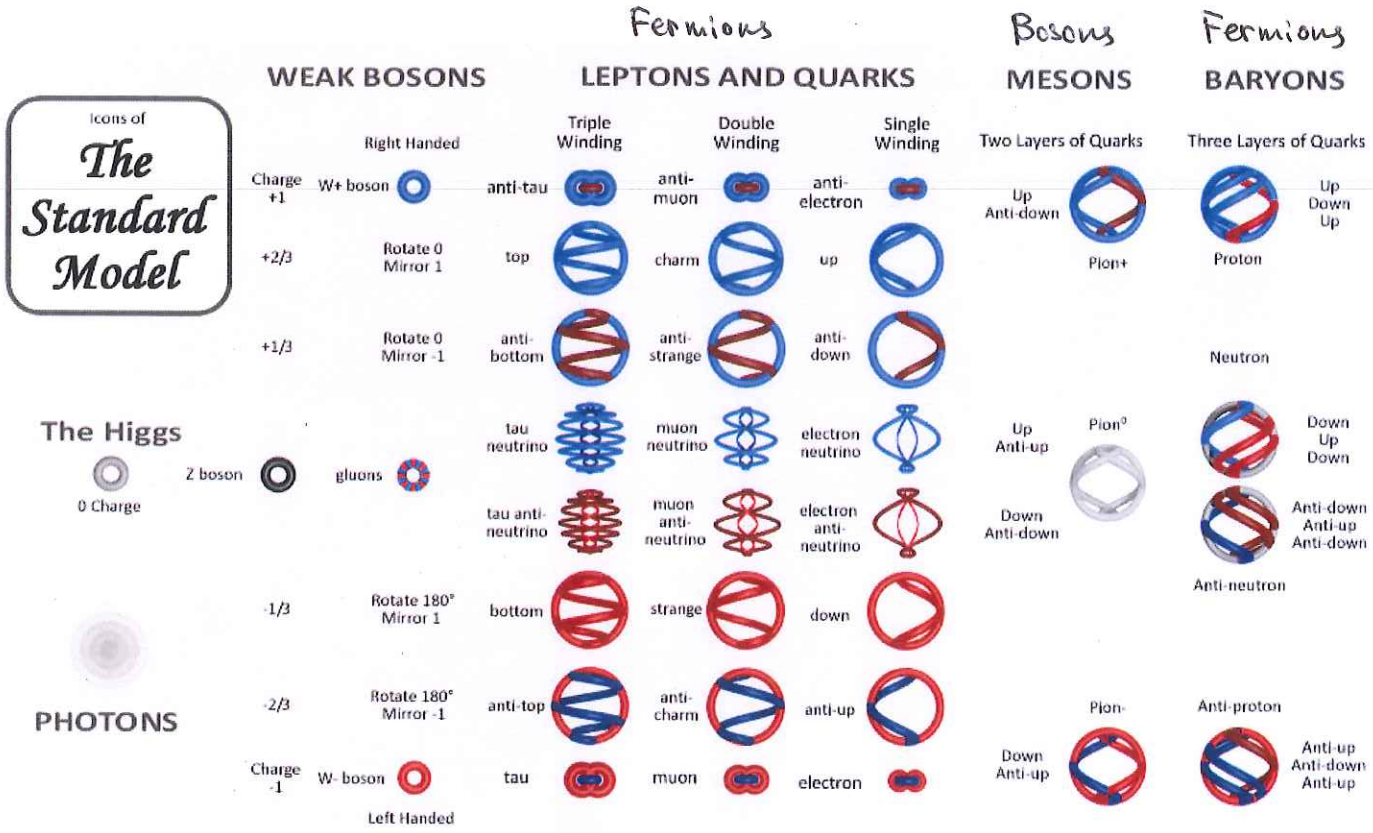
Fermions
Bosons
Fermions
WEAK BOSONS
LEPTONS AND QUARKS
MESONS
BARYONS
Icons of
The Standard Model
Right Handed
Triple Winding
Double Winding
Single Winding
Two Layers of Quarks
Three Layers of Quarks
Charge +1
W+ boson
anti-tau
anti-muon
anti-electron
Up
Anti-down
Pion+
Up
Down
Up
Proton
+2/3
Rotate 0 Mirror 1
top
charm
up
+1/3
Rotate 0 Mirror -1
anti-bottom
anti-strange
anti-down
Neutron
The Higgs
0 Charge
Z boson
gluons
tau neutrino
muon neutrino
electron neutrino
Up
Anti-up
Pion0
Down
Up
Down
tau anti-neutrino
muon anti-neutrino
electron anti-neutrino
Down
Anti-down
Anti-down
Anti-up
Anti-down
Anti-neutron
-1/3
Rotate 180° Mirror 1
bottom
strange
down
PHOTONS
-2/3
Rotate 180° Mirror -1
anti-top
anti-charm
anti-up
Pion-
Anti-proton
Down
Anti-up
Anti-up
Anti-down
Anti-up
Charge -1
W- boson
tau
muon
electron
Left Handed

COLD MOLECULES

A degenerate Fermi gas of polar molecules

Luigi De Marco[1,2], Giacomo Valtolina[1,2], Kyle Matsuda[1,2], William G. Tobias[1,2], Jacob P. Covey[1,2*], Jun Ye[1,2†]

Experimental realization of a quantum degenerate gas of molecules would provide access to a wide range of phenomena in molecular and quantum sciences. However, the very complexity that makes ultracold molecules so enticing has made reaching degeneracy an outstanding experimental challenge over the past decade. We now report the production of a degenerate Fermi gas of ultracold polar molecules of potassium-rubidium. Through coherent adiabatic association in a deeply degenerate mixture of a rubidium Bose-Einstein condensate and a potassium Fermi gas, we produce molecules at temperatures below 0.3 times the Fermi temperature. We explore the properties of this reactive gas and demonstrate how degeneracy suppresses chemical reactions, making a long-lived degenerate gas of polar molecules a reality.

Ultracold polar molecules are ideal candidates to realize a plethora of proposals in molecular and many-body physics. These include the development of chemistry in the quantum regime (*1*), the emulation of strongly interacting lattice spin models (*2–6*), the production of topological phases in optical lattices (*7–10*), the exploration of fundamental symmetries (*11–15*), and the study of quantum information science (*16–18*). Although magnetic atoms also exhibit long-ranged dipolar interactions and can be used to carry out these proposals (*19*, *20*), polar molecules offer more tunable, stronger interactions and additional degrees of freedom. A low-entropy, quantum degenerate sample is a prerequisite for many of these explorations.

The intrinsic complexity of molecules relative to atoms, owing to the additional rotational and vibrational degrees of freedom, has made their cooling to ultralow temperatures one of the most substantial experimental challenges in molecular physics (*21*). Although the direct laser cooling of certain diatomic molecules has progressed enormously in recent times so that magneto-optical (*22–25*) and pure optical (*26*) trapping have been demonstrated, phase space density in these systems remains many orders of magnitude away from degeneracy. To date, by far the coldest diatomic molecules have been made by cooling atoms to a few hundred nanokelvin (10^{-9} K) and coherently associating the ultracold atoms into deeply bound molecules by using a Fano–Feshbach resonance (*27*) followed by stimulated Raman adiabatic passage (STIRAP) (*28*).

Thus far, potassium-rubidium (KRb) (*28*), sodium-potassium (*29*, *30*), rubidium-cesium (*31*, *32*), sodium-rubidium (*33*), and lithium-sodium (*34*) have successfully been produced in deeply bound molecular states. Typically, such molecules can be produced in numbers ranging from hundreds to tens of thousands and at temperatures ranging from 250 to 600 nK. Reaching degeneracy in these experiments has been impeded by two major factors: the production of an adequate mixture of atoms to make a sufficient number of molecules and rapid molecular loss. Challenges in producing a suitable mixture can be technical or physical, such as the immiscibility of two Bose-Einstein condensates (BECs) (*35*). Molecules can be lost owing to chemical reactions; for example, KRb undergoes the exothermic $2KRb \rightarrow K_2 + Rb_2$ reaction (*36*, *37*). Even molecules predicted to have endothermic reactions show large inelastic loss caused by the complex nature of the scattering process, which is still being investigated (*29*, *33*, *38*). Indeed, the lowest-entropy samples of ground-state molecules have been produced in a three-dimensional (3D) optical lattice, in which chemical reactions cannot occur, with an entropy of just 2.2 k_B (Boltzmann constant) per particle (*39*); however, producing quantum degenerate molecules in a bulk gas has so far been an outstanding experimental goal.

Here, we report the production of 10^5 fermionic $^{40}K^{87}Rb$ molecules at 250 nK and as many as 2.5×10^4 molecules at 50 nK, the latter corresponding to $T/T_F = 0.3$, where T_F is the Fermi temperature. Moreover, we observed that quantum degeneracy is accompanied by a suppression of chemical reactions.

The efficiency of ultracold molecule production is limited at low temperatures by rapid three-body recombination of the atomic species as well as the spatial mismatch between atomic density distributions (*40–42*). For KRb, however, in the limit where the K number vastly exceeds the Rb number, these effects can be mitigated, and the conversion to molecules with respect to the minority species can be high (*42*). Furthermore, if the gases are deeply degenerate, the atoms' low entropy can be inherited by the molecules, resulting in a degenerate molecular gas (Fig. 1A). In our experiment, a large atom number before molecular association allowed us to take this approach and afforded us the flexibility to produce KRb molecules over a wide range of temperatures, densities, and T/T_F.

After collecting ~10^9 ^{87}Rb atoms and 7×10^7 ^{40}K atoms in a vapor-cell magneto-optical trap, we cooled the atoms to degeneracy by performing radiofrequency evaporation in an optically plugged quadrupole trap followed by evaporation in a crossed optical dipole trap (xODT) (*43*). After optical evaporation was complete, the xODT was recompressed so that K experienced harmonic trapping frequencies of $(\omega_x, \omega_y, \omega_z) = 2\pi \times (45, 250, 80)$ Hz, with gravity along the y direction. Trap frequencies are smaller by a factor of 0.72 and 0.79 for Rb and KRb, respectively, owing to differences in mass and AC polarizability. Slices through atomic column–integrated density distributions after 16 ms time of flight (TOF) for three representative conditions are shown in Fig. 1B, top, and the corresponding numbers are given in Table 1. Among a number of technical improvements that allowed us to produce a deeply degenerate mixture with a large number of atoms, a key advance was the implementation of Λ-enhanced gray molasses on the D_1 ($4^2S_{1/2} \rightarrow 4^2P_{1/2}$) line of K (*44*) as well as the D_2 ($5^2S_{1/2} \rightarrow 5^2P_{3/2}$) line of Rb (*45*).

We produced ground-state KRb molecules by sweeping a magnetic field through an interspecies Fano-Feshbach resonance at B = 546.6 G to create weakly bound Feshbach molecules (Fig. 1A) (*28*). The molecules were then coherently transferred to the ground state by using STIRAP with ~90% efficiency. We conducted the experiments described here at zero electric field. The difference in trapping frequencies between molecules and atoms resulted in all three species having different equilibrium positions because of gravitational sag (*46*). Even though the molecules had the same initial temperature as the atoms, the initial nonequilibrium position set the molecules in motion, and the gas rapidly heated up as potential energy was converted to kinetic energy. To mitigate this effect, before molecule production a 1D optical lattice of 30 molecular recoil energies was turned on against gravity. This ensured that the molecules and atoms were at equilibrium at the same position in the corrugated potential. After molecules were produced, unpaired atoms were quickly blasted away with resonant light (*43*), the lattice was then ramped off in 5 ms, and no spatial oscillations or rapid heating were observed.

By varying the initial temperature and atomic number ratio, we generated molecular gases ranging from T/T_F greater than 1 to less than

[1]JILA, National Institute of Standards and Technology (NIST) and University of Colorado, Boulder, CO 80309, USA. [2]Department of Physics, University of Colorado, 440 UCB, Boulder, CO 80309, USA.
*Present address: Department of Physics, California Institute of Technology, 1200 East California Boulevard, Pasadena, CA 91125, USA.
†Corresponding author. Email: ye@jila.colorado.edu

0.3. Three representative conditions are summarized in Table 1, and slices through molecular column density distributions after 10 ms TOF are shown in Fig. 1B, bottom; each molecular distribution shown was produced from the atomic conditions in Fig. 1B, top. Over this range, the average molecular density varies from 0.5×10^{12} to 2×10^{12} cm^{-3}.

At low T/T_F, the effects of degeneracy on the molecular velocity distribution after TOF are clear. Two-dimensional absorption images were collected and fit (*43*); the azimuthally averaged density profile of a cloud of KRb molecules after 10 ms TOF is shown in Fig. 2A. The profile is well fit by a Fermi–Dirac distribution [Fig. 2A, top, blue curve; $T/T_F = 0.31(2)$], whereas the classical Maxwell–Boltzmann distribution (Fig. 2A, top, red curve) overestimates the density at the center of the cloud and underestimates it in the wings. This is evident in the fit residuals (Fig. 2A, bottom), where the classical residuals exhibit ripples that are a hallmark of Fermi degeneracy (*47*). A Maxwell-Boltzmann fit to the wings of the profile (Fig. 2A, top, green curve), where the gas looks essentially classical, captures the temperature of the molecules but deviates at the center of the cloud.

The classical fit to the entire cloud systematically overestimates the temperature compared with the Fermi-Dirac fit because the Pauli exclusion principle prevents the multiple occupancy of low-energy states. The difference between the temperatures measured with the two fits is a strong indicator of the degree of quantum degeneracy (*47*). The normalized difference between these, $\delta U/U_{Cl} = 1 - T/T_{Cl}$, is shown in Fig 2B for KRb as a function of T/T_F, where T_{Cl} is the temperature determined from the Maxwell-Boltzmann fit. As T/T_F is decreased, the normalized energy shows a deviation from the classical value, and for the most degenerate molecular clouds we currently produce, the deviation is larger than 30%. For comparison, the same quantity is shown for K at several values of T/T_F; both sets of data show good agreement with the theoretical prediction for an ideal Fermi gas (Fig. 2B, solid line).

Given the T/T_F measured for K before molecular association, we expect an increase in the molecular T/T_F by roughly a factor of 3 to 4 based on the change in particle number and trap frequency. However, we typically measured values of T/T_F that were only a factor of 2.5 to 3 larger than that of K. At values of $T/T_F \lesssim 0.1$ for K, 85% of the Rb was condensed, and the Rb-to-K ratio was made to be roughly 1:10 (Table 1, third row) in order to minimize three-body recombination during magnetoassociation (*42*, *48*). Under these conditions, molecules were produced with $T/T_F \lesssim 0.3$. Because the Rb BEC was fairly localized to the center of the K cloud (Fig. 1B), molecules were only produced in the lowest-entropy part of the Fermi sea (*49*), resulting in molecules that have a lower T/T_F than expected from uniform K conversion over the entire distribution. At such low temperatures, the conversion from Rb to Feshbach molecules can be as high as 50%, indicating that there is good local phase space overlap between K and the Rb condensate. Because the density of the BEC is much higher than that of the K Fermi gas, the local conversion efficiency of K atoms approaches unity. This is the same principle of strong phase space matching that allowed for the efficient production of ground-state molecules in a 3D optical lattice (*39*). By contrast, at high T/T_F, where we produce the largest absolute number of molecules, conversion is typically 15% of Rb (Table 1, first row).

We produced degenerate molecules by adiabatically sweeping the magnetic field through a Fano-Feshbach resonance followed by coherent transfer to the ground state with high efficiency. Because the first step occurs on time scales that are comparable with the inverse trap frequency, the Feshbach molecules were produced at thermodynamic equilibrium (*50*). After transferring molecules to the ground state, we did not observe any large-scale spatial dynamics, suggesting that the ground-state molecular gas remains close to equilibrium. This was corroborated by the measured momentum distribution (Fig. 2A) and expansion energy (Fig. 2B). Furthermore, because inelastic collisions are predicted to be accompanied by a comparable number of elastic, momentum-exchanging collisions (*51*), this thermodynamic state is essentially maintained over the lifetime of the gas, as evidenced by the persistence of a low T/T_F, which grows slowly with

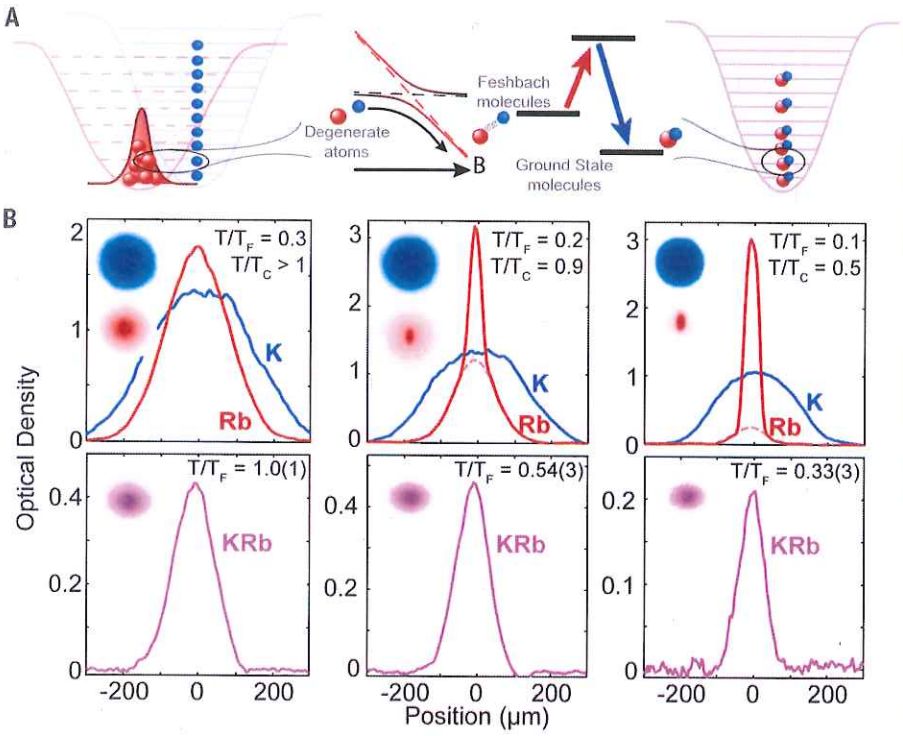

Fig. 1. Production of degenerate molecules. (**A**) Beginning with degenerate gases of Rb (red) and K (blue), Feshbach molecules are created by sweeping a magnetic field through a Fano-Feshbach resonance. The weakly bound molecules are coherently transferred to the ground state by using STIRAP. The resulting molecules reflect the degeneracy of their parent atoms. (**B**) Slices through images of atomic mixtures (two averages, 16 ms TOF, top) and ground-state molecules (four averages, 10 ms TOF, bottom) for molecular T/T_F ranging from 0.3 to 1 (right to left). (Inset) False-color 2D column density, with blue corresponding to K and red to Rb. Dashed red lines correspond to noncondensed component of Rb cloud. The TOF images reflect the differing momentum distributions of the atoms and molecules.

Table 1. Atom and molecule conditions corresponding to Fig. 1B.

T (nK)	Rb number	T/T_c	K number	T/T_F	KRb number	T/T_F
230	6×10^5	>1	1.2×10^6	0.3	$1.0(1) \times 10^5$	1.0(1)
110	2×10^5	0.9	1×10^6	0.2	$5.0(5) \times 10^4$	0.54(3)
50	7×10^4	0.5	5×10^5	0.1	$3.0(5) \times 10^4$	0.33(3)

time (fig. S2B) (*43*). This is further supported by the dependence of chemical reactions on degeneracy.

Given that KRb molecules are fermions, intermolecular scattering must occur in the *p*-wave channel because this is the lowest-energy antisymmetric collision channel. As such, the intermolecular potential (Fig. 3A) exhibits a centrifugal barrier through which molecules must tunnel in order to chemically react. According to the Bethe-Wigner threshold law (*52*, *53*), the tunneling rate (and therefore reaction rate) is proportional to the temperature, so that chemical reactions must slow down at low temperatures (*36*). Examples of density loss curves and their corresponding fits for two temperatures are shown in Fig. 3B. At low temperature, the density decays at a slower rate compared with at high temperature.

When a molecular collision leads to a reaction, the product molecules are ejected from the trap with high energy, leaving the remaining molecules unaffected because the mean free path is much larger than the size of the cloud. However, collisions tend to occur in the coldest, densest part of the cloud so that the lowest-energy molecules react and are lost preferentially, leading to anti-evaporation and an overall heating of the cloud. We typically observed heating linear in time, with rates ranging from $\dot{h}$ = 10 to 30 nK/s, which is slightly larger than a simple anti-evaporation model would suggest (*37*). However, this rate is small enough for the molecular T/T_F to remain close to its initial value over the molecules' lifetime.

The reduction of density is determined by both the loss of KRb molecules and the increase in temperature. We fit our data to a simple two-body model that includes the effect of heating (*36*)

$$\frac{dn}{dt} = -\beta n^2 - \frac{3}{2}\frac{n}{T}\frac{dT}{dt} \quad (1)$$

where n is the average classical molecular density of the bulk gas; the temperature is a measured, linear function of time, $T = T_0 + \dot{h}t$; and β is the two-body loss coefficient. Because two-particle threshold behavior predicts $\beta = bT$, the fitting of the data with Eq. 1 allows us to determine b (*43*).

Measurements of β as a function of initial molecular temperature are shown in Fig. 4A. Data points with a blue face correspond to $T/T_F \leq 0.6$, and those with a red face correspond to $T/T_F > 0.6$; the solid red curve is the value predicted by multichannel quantum defect theory (MQDT), based on a previously published ab initio calculation of the van der Waals coefficient, C_6 (*36*, *54*). The points with $T/T_F > 0.6$ follow the predicted MQDT trend closely, but those with $T/T_F \leq 0.6$ show deviations at all temperatures. Considering β/T, we observed a trend that is only dependent on T/T_F and not initial temperature. We found that at $T/T_F \leq 0.6$, β/T shows a strong deviation from the Bethe-Wigner threshold law, whereas above $T/T_F = 0.6$, β/T is constant, with a measured value of $\beta/T = 0.84(6) \times 10^{-5}$ cm^3 s^{-1} K^{-1} (Fig. 4B, black line, error range shown in gray). This value is in excellent agreement with the predicted MQDT value (*36*, *54*) of $\beta/T = 0.8(1) \times 10^{-5}$ cm^3 s^{-1} K^{-1} (Fig. 4B, red line). Our value is somewhat lower than the previously measured value of $\beta/T = 1.2(3) \times 10^{-5}$ cm^3 s^{-1} K^{-1} (*36*), with the discrepancy likely arising from the use of the corrugated potential to suppress gravitational sag in the current experiment.

Below $T/T_F = 0.6$, the measured β/T drops to values as low as $0.21(8) \times 10^{-5}$ cm^3 s^{-1} K^{-1}. A possible explanation for this observed deviation from a constant value is the change in density correlations as the gas becomes deeply degenerate. For a classical gas, the density sets the length scale of interparticle separation, which is much larger than the deBroglie wavelength, Λ. In this case, large density fluctuations occur on the molecular scale, and two particles can easily find a configuration to scatter in the *p*-wave channel. In a degenerate Fermi gas, however, the probability of finding two molecules within a short distance of each other decreases as T/T_F is lowered because of antibunching, with the average interparticle spacing being set by the deBroglie wavelength itself and ultimately by the Fermi wave vector, $2\pi/k_F$. This is the same physical phenomenon that gives rise to the Pauli pressure and reduced compressibility of a Fermi gas. This would cause an effective blockade that results in reduced density fluctuations (*55*–*57*) so that *p*-wave scattering and chemical reactions are suppressed beyond the Bethe-Wigner prediction. The suppressed collision rate manifests itself within our model as a reduction in the measured β/T for the bulk gas, although the true two-body reaction rate constant is unaffected by degeneracy for any given molecular collision.

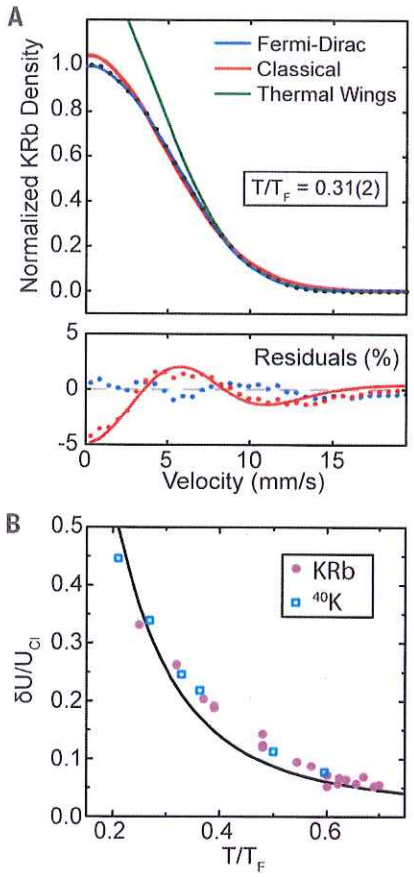

Fig. 2. Signatures of quantum degeneracy. (**A**) (Top) An azimuthally averaged molecular density profile with $T/T_F = 0.31(2)$ fit to a Fermi–Dirac distribution (blue curve) and a classical Maxwell-Boltzmann distribution (red curve). (Bottom) The fit residuals show the deviation of the classical fit (red points) characteristic of degeneracy; the solid curve corresponds to the difference of the residuals. Fitting only the wings of the cloud to a Maxwell-Boltzmann distribution (top, green curve) accurately captures the temperature but overestimates the density in the center. (**B**) The deviation of the internal energy of the molecular gas from its classical value grows as T/T_F is reduced. The solid curve is the expected result for an ideal Fermi gas, and the results for K are shown for comparison.

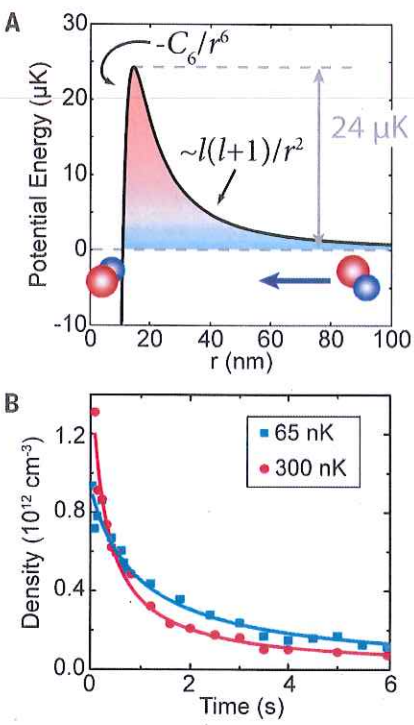

Fig. 3. Intermolecular reactions. (**A**) The intermolecular *p*-wave (l = 1) scattering potential for KRb (*36*). Molecules can react once they have tunneled through the barrier. (**B**) As reactions occur, molecular density (shown at two temperatures) decays according to a two-body rate law. The rate constant decreases with decreasing temperature in accordance with the Bethe-Wigner threshold law.

This effect is captured in the average relative number density fluctuation $\langle \delta n^2(r) \rangle / \langle n(r) \rangle$, which is shown as a blue line in Fig. 4B as a function of T/T_F. The curve is scaled to the MQDT value of β/T for $T/T_F > 1$ but otherwise has no fitting parameters. That this simple consideration qualitatively describes the change in reaction rate suggests that the reduced particle fluctuations correspondingly reduce the probability of two molecules colliding, resulting in a suppression of chemical reactions. Density fluctuations are most strongly suppressed in the center of the trap (*43*), where the majority of chemical reactions occur, which is a possible explanation for why some points fall below the expected fluctuation suppression curve. Similar suppression of loss caused by strong correlations has been observed in the three-body recombination rate of a 1D Bose gas in which the particles have undergone fermionization (*58*). Furthermore, this effect is reminiscent of the reduction of the elastic *s*-wave collision rate observed in fermionic atoms (*59*, *60*); however, in the elastic case, the reduction of the elastic cross section is attributed to the unavailability of empty states to scatter into, which is not relevant for inelastic collisions.

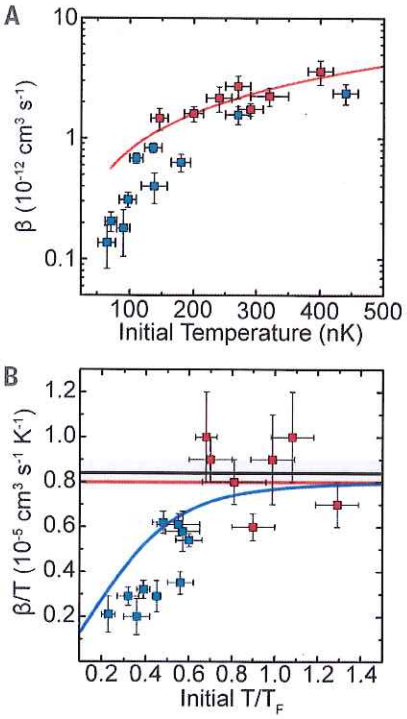

Fig. 4. Temperature dependence of reaction rate constants. (**A**) The reaction rate constant β for initial temperatures ranging from T = 70 to 450 nK. Solid blue points correspond to $T/T_F \leq 0.6$, and solid red points correspond to $T/T_F > 0.6$. The red curve is the value expected from MQDT. (**B**) Temperature-normalized reaction rate constants from (A) as a function of degeneracy. The measured β/T, as determined by fitting the average density to the solution of Eq. 1, appears to decrease sharply when $T/T_F < 0.6$ owing to the suppression of fluctuations. The solid black line and gray bar are the average β/T for $T/T_F > 0.6$ and corresponding error range. The red line is the MQDT value, and the blue curve is the average relative density fluctuations.

Although the qualitative agreement between the data and the suppression of density fluctuations is suggestive, a complete theory must treat the many-body nature of the degenerate gas within which the chemical reactions are taking place. In particular, it is important to consider the degree to which molecules thermalize after some are lost to chemical reactions. Furthermore, as T/T_F is decreased well below 0.3, collisions will be dominated by molecules near the Fermi surface so that the mean relative collision energy will deviate from the classical equipartition value to the quantum value of $\frac{3}{4}k_B T_F$ per particle.

The production of a degenerate Fermi gas of polar molecules opens previously unexplored paths in ultracold molecular science. In a bulk gas, we now have the opportunity to study chemical reactions in a regime where quantum degeneracy and quantum fluctuations compete with classical chemical reaction dynamics. Furthermore, this work shows great promise for the exploration of degenerate molecules in electric fields, where the strong dipole-dipole interaction dominates. In this limit, we expect to see interaction-induced effects such as the deformation of the Fermi surface and the development of exotic many-body correlations.

REFERENCES AND NOTES

1. L. D. Carr, D. DeMille, R. V. Krems, J. Ye, *New J. Phys.* **11**, 055049 (2009).
2. A. Micheli, G. K. Brennen, P. Zoller, *Nat. Phys.* **2**, 341–347 (2006).
3. K. Osterloh, N. Barberán, M. Lewenstein, *Phys. Rev. Lett.* **99**, 160403 (2007).
4. H. P. Büchler *et al.*, *Phys. Rev. Lett.* **98**, 060404 (2007).
5. A. V. Gorshkov *et al.*, *Phys. Rev. Lett.* **107**, 115301 (2011).
6. M. A. Baranov, M. Dalmonte, G. Pupillo, P. Zoller, *Chem. Rev.* **112**, 5012–5061 (2012).
7. N. R. Cooper, G. V. Shlyapnikov, *Phys. Rev. Lett.* **103**, 155302 (2009).
8. N. Y. Yao *et al.*, *Phys. Rev. Lett.* **110**, 185302 (2013).
9. S. V. Syzranov, M. L. Wall, V. Gurarie, A. M. Rey, *Nat. Commun.* **5**, 5391 (2014).
10. D. Peter *et al.*, *Phys. Rev. A* **91**, 053617 (2015).
11. M. G. Kozlov, L. N. Labzowsky, *J. Phys. B* **28**, 1933–1961 (1995).
12. V. V. Flambaum, M. G. Kozlov, *Phys. Rev. Lett.* **99**, 150801 (2007).
13. J. J. Hudson *et al.*, *Nature* **473**, 493–496 (2011).
14. J. Baron *et al.*, *Science* **343**, 269–272 (2014).
15. W. B. Cairncross *et al.*, *Phys. Rev. Lett.* **119**, 153001 (2017).
16. A. André *et al.*, *Nat. Phys.* **2**, 636–642 (2006).
17. S. F. Yelin, K. Kirby, R. Côté, *Phys. Rev. A* **74**, 050301 (2006).
18. K.-K. Ni, T. Rosenband, D. D. Grimes, *Chem. Sci.* **9**, 6830–6838 (2018).
19. T. Lahaye, C. Menotti, L. Santos, M. Lewenstein, T. Pfau, *Rep. Prog. Phys.* **72**, 126401 (2009).
20. K. Aikawa *et al.*, *Phys. Rev. Lett.* **112**, 010404 (2014).
21. J. L. Bohn, A. M. Rey, J. Ye, *Science* **357**, 1002–1010 (2017).
22. M. T. Hummon *et al.*, *Phys. Rev. Lett.* **110**, 143001 (2013).
23. J. F. Barry, D. J. McCarron, E. B. Norrgard, M. H. Steinecker, D. DeMille, *Nature* **512**, 286–289 (2014).
24. L. Anderegg *et al.*, *Phys. Rev. Lett.* **119**, 103201 (2017).
25. S. Truppe *et al.*, *Nat. Phys.* **13**, 1173–1176 (2017).
26. L. Anderegg *et al.*, *Nat. Phys.* **14**, 890–893 (2018).
27. C. Chin, R. Grimm, P. Julienne, E. Tiesinga, *Rev. Mod. Phys.* **82**, 1225–1286 (2010).
28. K. K. Ni *et al.*, *Science* **322**, 231–235 (2008).
29. J. W. Park, S. A. Will, M. W. Zwierlein, *Phys. Rev. Lett.* **114**, 205302 (2015).
30. F. Seeßelberg *et al.*, *Phys. Rev. A* **97**, 013405 (2018).
31. T. Takekoshi *et al.*, *Phys. Rev. Lett.* **113**, 205301 (2014).
32. P. K. Molony *et al.*, *Phys. Rev. Lett.* **113**, 255301 (2014).
33. M. Guo *et al.*, *Phys. Rev. Lett.* **116**, 205303 (2016).
34. T. M. Rvachov *et al.*, *Phys. Rev. Lett.* **119**, 143001 (2017).
35. L. Reichsöllner, A. Schindewolf, T. Takekoshi, R. Grimm, H.-C. Nägerl, *Phys. Rev. Lett.* **118**, 073201 (2017).
36. S. Ospelkaus *et al.*, *Science* **327**, 853–857 (2010).
37. K. K. Ni *et al.*, *Nature* **464**, 1324–1328 (2010).
38. M. Mayle, G. Quéméner, B. P. Ruzic, J. L. Bohn, *Phys. Rev. A* **87**, 012709 (2013).
39. S. A. Moses *et al.*, *Science* **350**, 659–662 (2015).
40. J. Herbig *et al.*, *Science* **301**, 1510–1513 (2003).
41. J. J. Zirbel *et al.*, *Phys. Rev. A* **78**, 013416 (2008).
42. T. D. Cumby, R. A. Shewmon, M.-G. Hu, J. D. Perreault, D. S. Jin, *Phys. Rev. A* **87**, 012703 (2013).
43. Materials and methods are available as supplementary materials.
44. D. Rio Fernandes *et al.*, *Europhys. Lett.* **100**, 63001 (2012).
45. S. Rosi *et al.*, *Sci. Rep.* **8**, 1301 (2018).
46. G. Delannoy *et al.*, *Phys. Rev. A* **63**, 051602 (2001).
47. B. DeMarco, D. S. Jin, *Science* **285**, 1703–1706 (1999).
48. J. J. Zirbel *et al.*, *Phys. Rev. Lett.* **100**, 143201 (2008).
49. T.-L. Ho, Q. Zhou, *Proc. Natl. Acad. Sci. U.S.A.* **106**, 6916–6920 (2009).
50. M. Greiner, C. A. Regal, D. S. Jin, *Nature* **426**, 537–540 (2003).
51. Z. Idziaszek, G. Quéméner, J. L. Bohn, P. S. Julienne, *Phys. Rev. A* **82**, 020703 (2010).
52. E. P. Wigner, *Phys. Rev.* **73**, 1002–1009 (1948).
53. H. R. Sadeghpour *et al.*, *J. Phys. B* **33**, R93–R140 (2000).
54. Z. Idziaszek, P. S. Julienne, *Phys. Rev. Lett.* **104**, 113202 (2010).
55. T. Rom *et al.*, *Nature* **444**, 733–736 (2006).
56. C. Sanner *et al.*, *Phys. Rev. Lett.* **105**, 040402 (2010).
57. T. Müller *et al.*, *Phys. Rev. Lett.* **105**, 040401 (2010).
58. B. Laburthe Tolra *et al.*, *Phys. Rev. Lett.* **92**, 190401 (2004).
59. B. DeMarco, S. B. Papp, D. S. Jin, *Phys. Rev. Lett.* **86**, 5409–5412 (2001).
60. K. Aikawa *et al.*, *Phys. Rev. Lett.* **113**, 263201 (2014).
61. L. De Marco *et al.*, Replication data for: A degenerate Fermi gas of polar molecules. Harvard Dataverse, version 1.0 (2019).

ACKNOWLEDGMENTS

We dedicate this work to the memory of Deborah Jin, whose brilliance and passion inspire us all. We thank J. Bohn, E. Cornell, C. Greene, P. He, M. Holland, S. Moses, and A. M. Rey for useful discussions. **Funding:** This work is supported by NIST, Air Force Office of Scientific Research–Multidisciplinary University Research Initiative (MURI), Army Research Office–MURI, and the NSF JILA Physics Frontier Center (NSF PHY-1734006). **Author contributions:** All authors contributed to carrying out the experiments, interpreting the results, and writing the manuscript. **Competing interests:** The authors declare that they have no competing financial interests. **Data and materials availability:** Data from the main text and supplementary materials are available through the Harvard Dataverse at (*61*).

SUPPLEMENTARY MATERIALS

www.sciencemag.org/content/363/6429/853/suppl/DC1
Materials and Methods
Figs. S1 to S3

9 July 2018; accepted 4 January 2019
Published online 17 January 2019
10.1126/science.aau7230